

**Calcium silicate against clay brick masonry  
an experimental comparison of the in-plane behaviour during light damage**

Korswagen, Paul A.; Longo, Michele; Rots, Jan G.

**DOI**

[10.1007/s10518-020-00803-5](https://doi.org/10.1007/s10518-020-00803-5)

**Publication date**

2020

**Document Version**

Final published version

**Published in**

Bulletin of Earthquake Engineering

**Citation (APA)**

Korswagen, P. A., Longo, M., & Rots, J. G. (2020). Calcium silicate against clay brick masonry: an experimental comparison of the in-plane behaviour during light damage. *Bulletin of Earthquake Engineering*, 18(6), 2759–2781. <https://doi.org/10.1007/s10518-020-00803-5>

**Important note**

To cite this publication, please use the final published version (if applicable).  
Please check the document version above.

**Copyright**

Other than for strictly personal use, it is not permitted to download, forward or distribute the text or part of it, without the consent of the author(s) and/or copyright holder(s), unless the work is under an open content license such as Creative Commons.

**Takedown policy**

Please contact us and provide details if you believe this document breaches copyrights.  
We will remove access to the work immediately and investigate your claim.



# Calcium silicate against clay brick masonry: an experimental comparison of the in-plane behaviour during light damage

Paul A. Korswagen<sup>1</sup> · Michele Longo<sup>1</sup> · Jan G. Rots<sup>1</sup>

Received: 1 August 2019 / Accepted: 10 February 2020 / Published online: 15 February 2020  
© The Author(s) 2020

## Abstract

The north of the Netherlands is prone to frequent, light earthquakes linked to economical losses and societal unrest due to the induced seismicity in the region. These light earthquakes produce correspondingly low values of in-plane drift on the typical masonry structures of the region, many of which are built with cavity walls composed of an inner, load-bearing calcium-silicate masonry leaf, and an outer, exposed fired-clay masonry veneer. To assess the resulting damage from the lighter earthquakes, it is thus necessary to understand the difference in behaviour of the inner and the outer masonry leaves when exposed to the same drift values. Experimental tests of replicated, full-scale calcium-silicate brick walls and spandrels are detailed herein and compared to previously tested clay masonry samples. A purposely developed, scalar damage parameter is used to assess the width, number and length of the cracks to objectively quantify damage. High resolution digital image correlation is used to accurately monitor the initiation and propagation of cracks. The experiments reveal that calcium-silicate samples exhibit slightly greater damage than clay samples when subjected to the same in-plane drift. From the tests, drift values for light damage or ‘damage state one’ are set between 0.15 and 0.65‰ for the type of wall tested. Moreover, in these tests, cracks in calcium-silicate samples were significantly more likely to split brick units, whereas cracks in the type of clay samples employed, always followed the masonry joints. This fundamental difference in the light-damage behaviour between the two materials is of importance when considering the perception of damage, the strategies and cost of the repairs, and the strategies for strengthening of masonry structures with cavity walls resembling the type of masonry tested herein.

**Keywords** Calcium silicate · Clay masonry · Light damage · Cracks · DIC

## 1 Introduction

The extraction of natural gas in the province of Groningen in the north of the Netherlands has caused a number of small induced seismic events which have produced vibrations with peak ground acceleration values measured in the order of 0.1 g (see

---

✉ Paul A. Korswagen  
P.A.KorswagenEguren@tudelft.nl

<sup>1</sup> Delft University of Technology, Delft, The Netherlands

for instance, den Bezemer and van Elk 2018; or, NAM 2016). These earthquakes are suspected of having the potential to cause light damage to the ubiquitous, unreinforced masonry structures of the region, which were not designed to sustain seismic loading. In particular, the repeated exposure of the structures to these events triggers questions about the accumulation of damage (see for example Sarhosis et al. 2019; Van Staalduinen et al. 2018).

The ultimate-limit-state capacity of these structures against possible, larger earthquakes has been extensively assessed as a first priority to evaluate the individual risk (see e.g. Crowley et al. 2018; Graziotti et al. 2017; Esposito et al. 2018; Messali et al. 2018). The focus is now broadened to the behaviour of the structures under light damage. The present study considers the resulting light damage, in this context denoted as damage state one (DS1), see for instance de Vent et al. (2011). Where near-collapse and ultimate limit states received much attention, the literature in the field of aesthetic, light damage remains scarce. Furthermore, in Groningen, light damage appears to be limited to in-plane effects with no clear evidence of damage due to out-of-plane effects (Van Staalduinen et al. 2018).

Masonry in the region is typically unreinforced and consists of baked-clay bricks arranged in single- or double-wythe walls as detailed by Thijssen (1999), see also Hendry (2001). Newer structures, predominantly in the period after 1970, employ cavity walls consisting of an outer clay-brick façade and an inner calcium-silicate load-bearing wall, both in a running stretcher bond scheme and connected to each other using thin steel ties. The older calcium-silicate walls are built using bricks, but newer structures also sport larger blocks, elements, or panels; this study is however limited to bricks, but Jonaitis et al. (2009) for example, treat blocks while Jafari and Esposito (2019) also consider elements. In this light, an earlier study conducted at Delft University of Technology has focused on providing a first insight into the light damage behaviour of the clay walls as these are part of both the older and newer structures, albeit the study uses masonry replicating the material properties of the older clay-brick walls, see Korswagen et al. (2019). Accordingly, studying masonry walls of calcium-silicate brick and comparing these to the already-tested clay-brick walls is hence a sensible follow-up, one which is treated in this paper. In fact, calcium-silicate walls are perhaps more vulnerable to light damage than the older clay-brick walls as is also discussed herein. Note however, that the measure of light damage focuses more on the aesthetic aspect of the damage instead of the structurally-relevant measure of higher damage states. Here, the strength (lateral force capacity) of the calcium walls is undoubtedly higher when compared to similar and similarly loaded clay-brick walls as has been explored by studies into the ultimate-limit state of the structures: see Messali and Rots (2018), Magenes et al. (2012), or Graziotti et al. (2016).

The comparison of light damage behaviour between clay and calcium-silicate brick walls is done on the basis of experimental tests on similar full-scale walls and spandrel tests. The two materials are compared in terms of their stiffness, strength, intensity of damage at equal values of drift, and the overall significance of the damage. The reader is referred to Korswagen et al. (2019) for details about the testing of the clay-brick walls and spandrels, as in this article, only the results of the calcium-silicate walls are presented, discussed and later compared with their clay counterparts. Accordingly, chapter 2 presents an overview of the setup of the tests and chapter 3 presents the results. Then, chapter 4 carries out the comparison to the previously-tested clay walls and chapter 5 sums up the main conclusions of this text.

## 2 Setup of laboratory tests

Two nominally identical full-scale walls (see Fig. 1.a) were identically tested in their plane under a small, constant pre-compression stress of 0.12 MPa and a displacement-controlled, cyclically-increasing lateral drift. The walls were single-Wythe and approximately 3.1 m in width and 2.7 m in height. A window opening, positioned asymmetrically in the wall, was included to better mimic field cases where cracks are usually seen around windows (corners), see for instance Grünthal et al. (1998). The wall was fixed to a bottom steel beam and to a top steel beam, the latter of which was allowed to displace and rotate in the plane of the wall thus simulating a cantilever boundary condition. The lateral edges of the walls were free to minimise the complexity of the tests while simulating typical structural cases where structural or infill walls are only tied to neighbouring (transversal) walls without interlocking of bricks.

Additionally, five spandrel samples (Fig. 1b) were tested in a modified four-point bending setup under a crack mouth opening displacement (CMOD) controlled scheme. This setup allows for the possibility of applying one-way cyclic loading by employing counterweights (CW) aligned on the underside of the sample opposing the location of two hydraulic jacks (F). Additional details about the experimental setup of the walls can be found in Messali and Rots (2018), and about the setup of the spandrels in Korswagen et al. (2019). The specimens were built to replicate calcium-silicate brick masonry as found in the Groningen area. A characterisation campaign was conducted to establish the material properties of the existing masonry and build laboratory equivalents of these, see Jafari et al. (2017). The wall also included a reinforced concrete lintel which did not participate in the development of damage.

The loading protocol for the walls consisted of five incremental steps of one-way cyclic loading in the positive (or pull) direction, followed by another seven incremental steps two-way cyclic. Each step consisted of 30 cycles. The amplitude of the first step was 0.26‰ (lateral drift) and was increased 0.07‰ in every subsequent one-way cyclic step (until 0.55‰), and restarted at 0.26‰ at the beginning of the two-way cyclic portion of the protocol until finally reaching 0.70‰. A representation of the loading protocol, which was identical to the one used to test the clay-brick walls, is drawn in Fig. 2. The high number of small cycles included in the protocol are to mimic the effect of numerous light seismic or

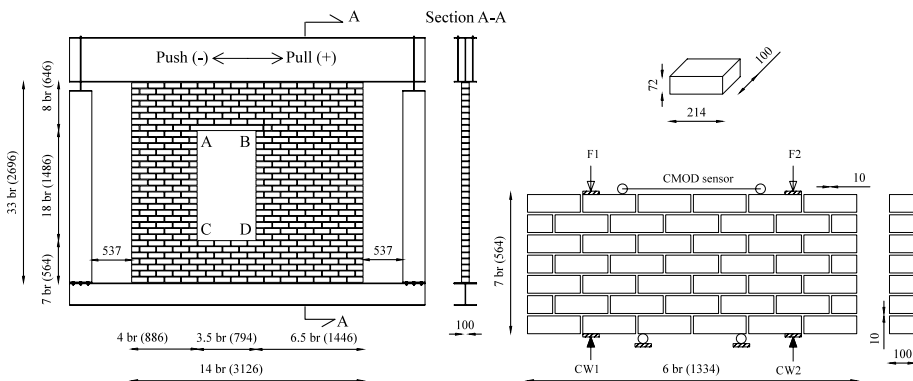


**Fig. 1** Left (a), dimensions of the full-scale wall; and right (b), dimensions and loading scheme of the spandrel specimens. Values in millimetres

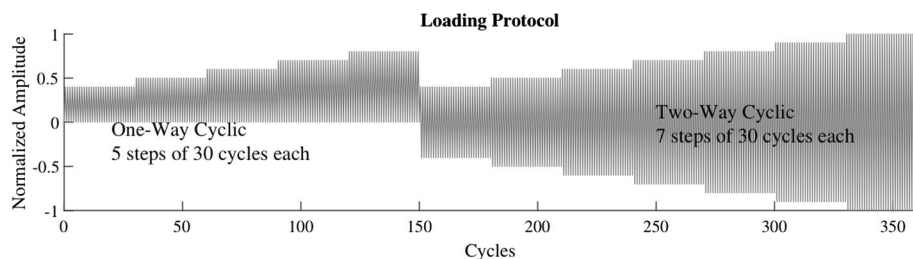
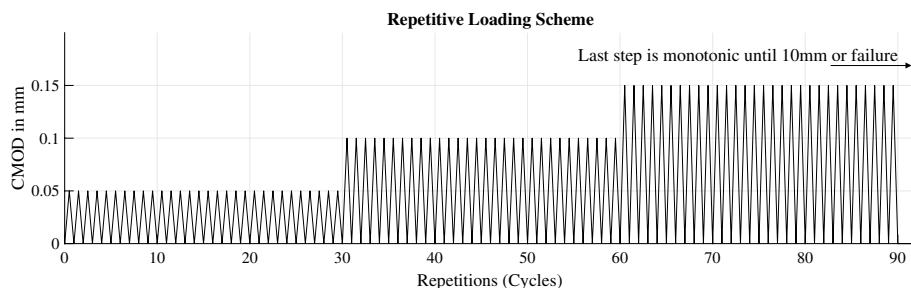


**Fig. 2** Loading protocol of the full-scale walls

other events, and were chosen to specifically allow the observation of (strength) degradation within each step. Whether these drift values will occur in real structures will depend on the structures themselves and the seismic events in the region. Nonetheless, light damage will occur around the small values employed herein (in comparison to standards). A more extensive description of the protocol can be found in Korswagen et al. (2019). See also Petry and Beyer (2015) and Messali and Rots (2018) for a comparison of expected drift limits.

The spandrels were tested under a one-way cyclic scheme where the CMOD was first repeated 30 times at values of 50  $\mu\text{m}$ , 100  $\mu\text{m}$ , and 150  $\mu\text{m}$  (for a total of 90 cycles) before being driven monotonically to 10 mm (though failure occurred before reaching this value). The repetitions had a lower boundary of a force of 1 kN to maintain stability in the system. Note also that the CMOD sensor was placed spanning the three top head joints to account for the possibility of a crack opening in any of these joints (Fig. 1b). See Fig. 3 for a representation of the loading protocol of the spandrels. A summary of the tested specimens and their protocols is given in Table 1.

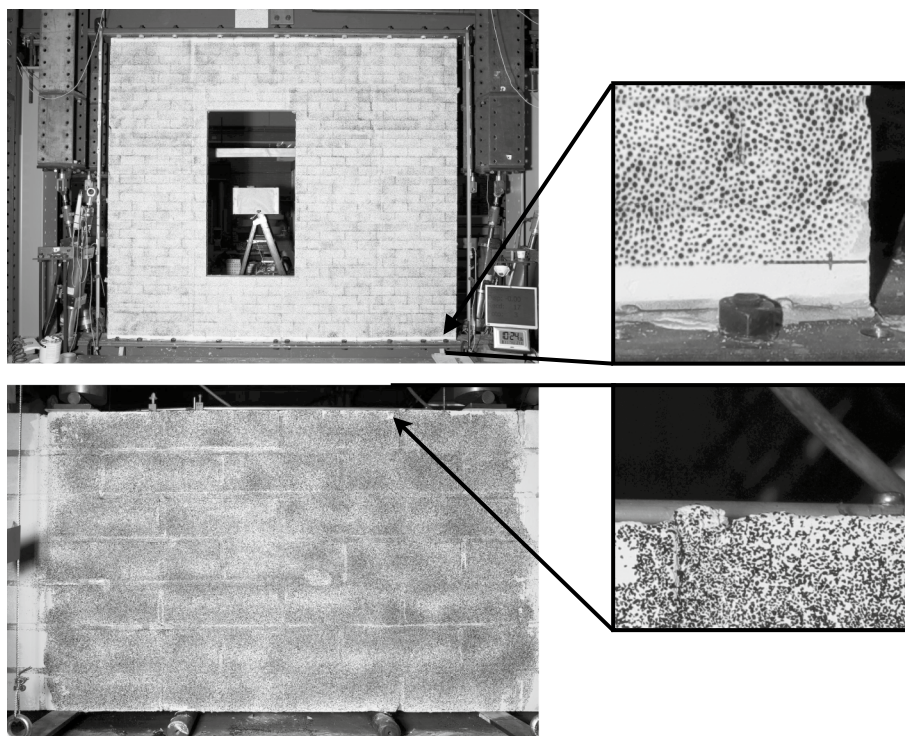
Both types of tests were monitored using the photogrammetry technique of Digital Image Correlation (DIC). The surface of the specimens was covered with a purposely-optimised random speckle pattern and photographed at specific time points throughout the tests (see Fig. 4). This allowed high-resolution measurement of the entire 2D, in-plane displacement field of the samples; in the case of the walls, approximately one million points were monitored at a distance of 2.8 mm between the points, and for the spandrels, 75,000 points at 2.4 mm distance were observed. The precision of the walls' measurement was 20  $\mu\text{m}$  while for the spandrels, 5  $\mu\text{m}$ . Additionally, traditional sensors and LVDTs were placed at the back of the wall and spandrels, and between the walls and the steel frames. Moreover,



**Fig. 3** Loading protocol of the spandrels

**Table 1** Summary of tests and specimens

Type	Name	Protocol	Control
Full-scale wall lateral, in-plane drift	TUD-component 49 TUD-component 50	5 × 30 one-way cyclic followed by 7 × 30 two-way cyclic	Drift (displacement) controlled
Spandrel (window bank of walls) modified 4-point bending test	Sample A Sample B Sample C Sample D Sample E	3 × 30 one-way cyclic followed by monotonic until failure	CMOD-controlled

**Fig. 4** Specimens of wall (top) and spandrel (bottom) with DIC pattern zoomed in

the out-of-plane displacement of the wall was monitored using two laser sensors pointing the the centre of the piers. DIC has been successfully employed to evaluate crack initiation and propagation in masonry, see for example Mojsilović and Salmanpour (2016). In this study, however, the propagation of cracks can be measured in between cycles to observe any increase in crack width. Then, the crack pattern at a given instance during the test is characterised with a damage parameter that determines the damage intensity based on the number, width, and length of the cracks following Eq. 1. The total of visible cracks is

expressed in one number such that the narrowest visible cracks with a width of 0.1 mm result in a value of around one ( $\Psi=1$ ), slightly larger cracks of close to 1 mm width correspond to two ( $\Psi=2$ ) and cracks of approximately 4 mm in width give a value of three ( $\Psi=3$ ). This range corresponds to light damage (DS1) as defined herein. Additional information regarding this parameter can be found in Korswagen et al. (2018) and Korswagen et al. (2019).

$$\Psi = 2 \cdot n_c^{0.15} \cdot \hat{c}_w^{0.3} \quad \text{with} \quad \hat{c}_w = \frac{\sum_{i=1}^{n_c} c_{w,i}^2 \cdot c_{L,i}}{\sum_{i=1}^{n_c} c_{w,i} \cdot c_{L,i}} \quad (1)$$

where  $n_c$  is the number of cracks in the wall/specimen,  $\hat{c}_w$  is the width-weighted and length-averaged crack width (in mm) calculated with:  $c_w$  is the maximum crack width along each crack in mm,  $c_L$  is the crack length in mm, For  $n_c = 1$ ,  $\hat{c}_w = c_w$ . In this expression, the crack width of each crack is measured at their widest point.

### 3 Results of tests of calcium-silicate specimens

Both full-scale walls were incrementally displaced in-plane up to a drift of 0.7‰, which is low compared to drift associated with near-collapse in the order of 1–3%. Nevertheless, the walls exhibited considerable degradation in their cyclic force–displacement behaviour, see Fig. 5, left. Already after five one-way cyclic repetitions of the first imposed drift (0.26‰), the first wall had lost 2 kN of its peak lateral capacity (see Fig. 5b), which corresponds to about 7% of its strength. The right side of Fig. 5 shows thus the decline in peak force capacity (the absolute maximum attained in the positive and negative directions) for each consecutive cycle. Throughout the tests, a consistent decrease in peak force capacity can be observed for both walls of about 5% per step. Moreover, after the one-way test (initial 150 cycles with drift only in the positive direction and shaded in Fig. 5, right) had been finished and the initial positive drift was repeated, the walls showed a considerable reduction in strength of up to 30%: from approximately 25 to 17 kN, and from 24 to 18 kN for each wall respectively. Conversely, the capacity in the negative drift direction at the beginning of the two-way test was unaffected and began to degrade in a manner similar to that of the positive direction during the one-way test. Accordingly, for the first wall, the positive capacity showed almost no degradation during the two-way test, presumably because the one-way test had already damaged this direction; however, the second wall did show degradation but its capacity never exceeded what had been achieved during the one-way part of the test. Furthermore, both walls seemed to develop what would later have become the ultimate failure mechanism during the last step of the test; this is visible in all four graphs of Fig. 5. Both walls seem to accumulate significant lateral deformation leading to an increase in the hysteresis of Fig. 5a, c.

The force-drift and strength degradation of the wall throughout the test can be well traced to their behaviour and progressing damage which was accurately captured with DIC. Figure 6 shows the displacement field composed by tracking one million individual points; note that here the displacements have been magnified by 400 times and in reality no crack exceeded a width of 2.5 mm. During these observations, no lifting or rocking was detected in the walls and the out-of-plane deformations were negligible.

In Fig. 6a-1 (referring to step 1 in Fig. 6a, this notation continues) and Fig. 6b-1, the initiation of visible cracks can be appreciated. The protocol was designed such that the first



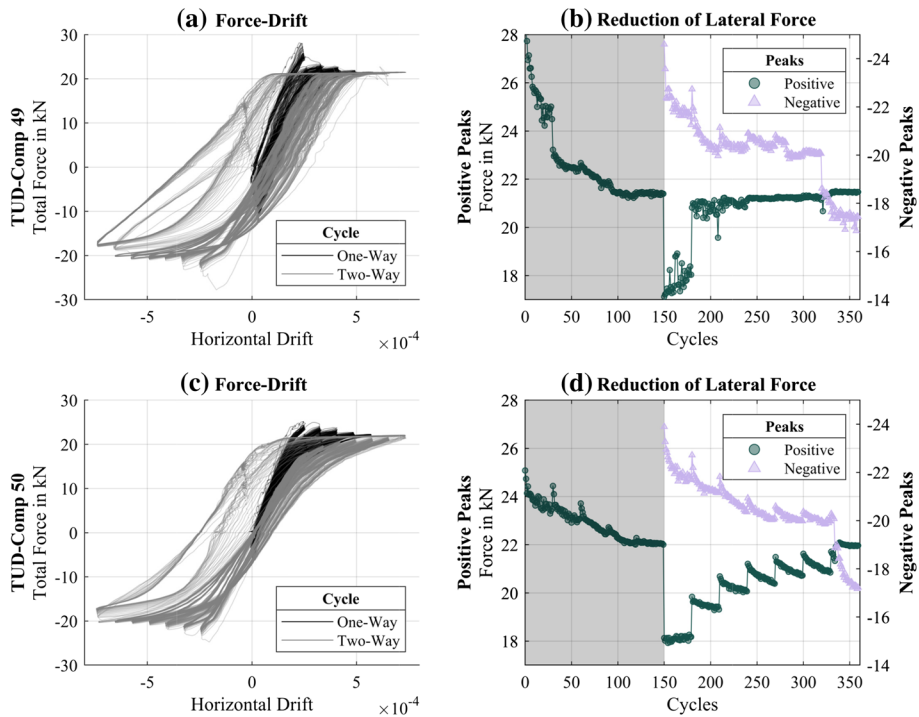


**Fig. 5** Force-drift curves and cyclic degradation graph for the full-scale walls: TUD-Comp49 in **a, b**, and TUD-Comp50 in **c, d**

step corresponded to the start of DS1. Yet, for the first wall, Comp49, Fig. 6a-2 shows that the top crack (A, see Fig. 1) has propagated fully through the pier in a diagonal manner. This is not the case for Comp50, where crack A runs horizontally to the edge of the wall in step 3, and while open, remains horizontally connected to the top spandrel throughout the entire test (no crack sliding displacement). Conversely, crack A leads to accumulated sliding for Comp49 and the pier becomes fully detached from step 11 onwards (Fig. 6a-11). This residual damage is then also clearly visible at the zero positions of Fig. 6a and hints at a mixed mode (mode I and mode II) behaviour for this crack. For Comp50, it is crack D the one to accumulate the most sliding as begins to show in Fig. 6b-9. The ultimate failure mechanism develops fully in Fig. 6a-10 for Comp49 comprising cracks A and B, and in Fig. 6b-11, the last step for Comp50, with crack B. It is remarkable that the walls, after this repeating damage, ultimately decompose in four rigid bodies which slide and rotate against each other, with little elastic deformation remaining.

The individual progression of the cracks and their representation of damage can also be extracted from the DIC data. This is shown in Fig. 7a where the crack width is plotted on the left axes and the damage parameter  $\Psi$  is measured on the right, the parameter is computed using the maximum crack width of each crack during each cycle. These graphs evidence the propagation of the cracks in every step, but also during certain steps, especially towards the end of the test. It can be observed that the behaviour of the cracks is linked as multiple cracks grow at the same time. During DS1 ( $\Psi < 3$ ), cracks grow from 0.1 mm up to 2 mm and most have similar widths at any given time. For Comp50, crack 3



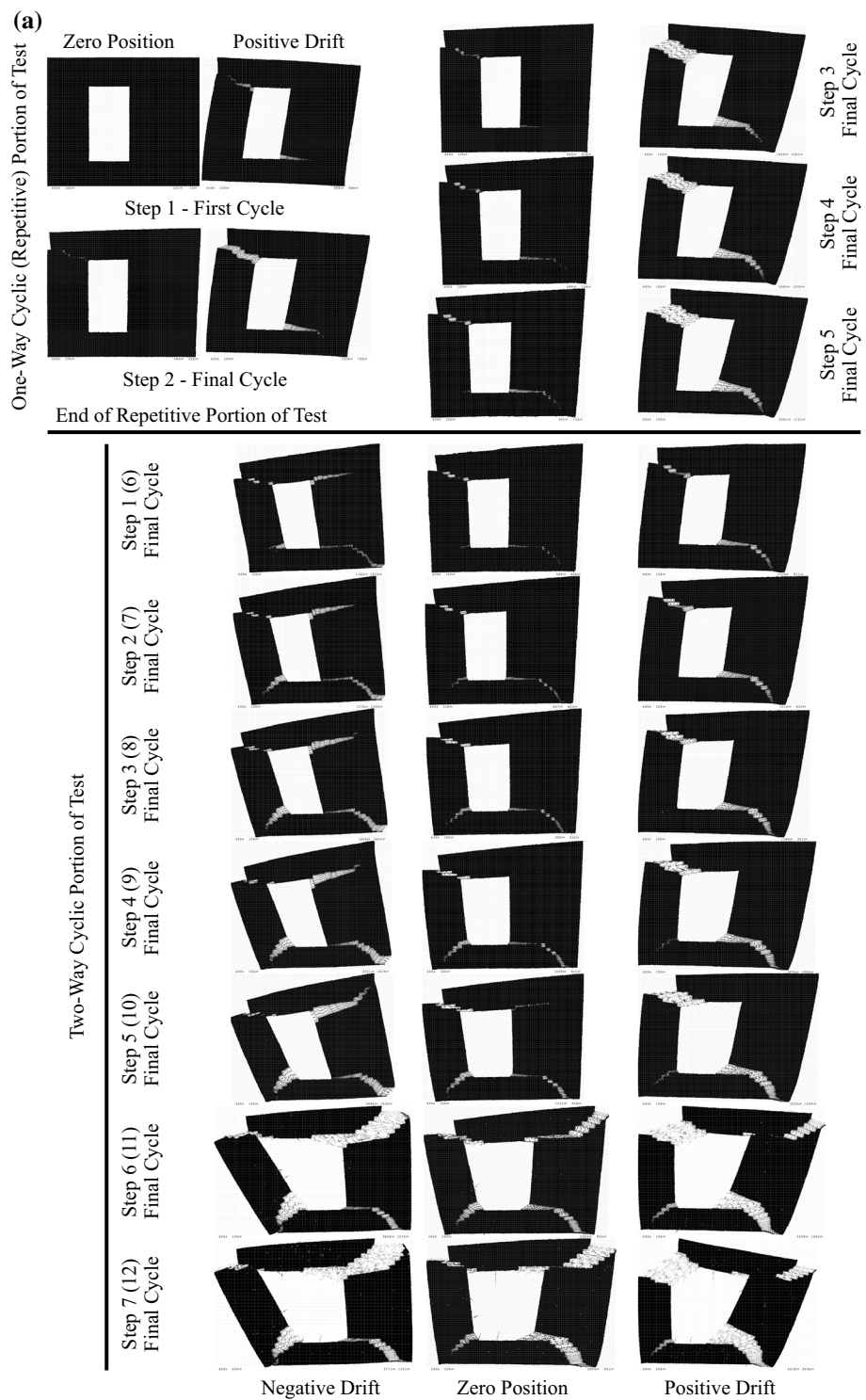
**Fig. 6** 400x magnified displacement field (deformed shape) for the **a** first wall, TUD-Comp49, **b** second wall, TUD-Comp50. Steps refer to the protocol of Fig. 2: 5 steps one-way cyclic (repetitive) followed by 7 steps two-way cyclic, (12) total steps

(C) propagated from both the outer edge of the wall during the one-way cyclic portion of the test as from the corner of the window later on. The propagation of the cracks is clearer in Fig. 7b where the length of the cracks (to a cut-off minimum crack width of 80  $\mu\text{m}$ ) is drawn. Here, the substantial increase in length within steps demonstrates that crack propagation must be (partly) responsible for the strength degradation observed in Fig. 5. Figure 7b also shows that crack 2 (A) is the first to propagate fully, revealing no growth in length already after the second step for both walls; then, crack 1 (D) reaches its full length at the beginning of the two-way portion of the test. This is presumably because both cracks are triggered by the one-way part of the test and hence experience a greater number of cycles.

It is also worth noting that cracks C and D, and also B for Comp50, run through bricks. This can be seen in the overview of Fig. 7 (and later Fig. 8), where, as cracks approach the edge of the wall, their paths become fully vertical instead of stair-case diagonal. Before these points, cracks follow the path of the mortar joints, and apparently, as the vertical weight of the wall rests on a few bricks when the wall is pushed laterally (see Fig. 6a-6 and -8 or Fig. 6b-9), the brick positioned in front of the vertical mortar joint at the edge of the crack is forced to split. For crack C, the split is fully vertical, while for crack D, the split is slightly inclined following the apparent path of the resultant force vector, suggesting that failure of the bricks is a mixture of bending and compression-induced tension-splitting (or compression-shear at the bed joint level). The path of the cracks is summed up in Fig. 8 overlaid on photographs of the wall.

The final crack pattern during the spandrel tests is also depicted in Fig. 8 and shown to run through both mortar joints and bricks; in these cases however, failure of the bricks is not associated with compression-induced splitting but corresponds to flexural failure of the bricks and in general, the specimens. The failure occurred in such a brittle manner that in two of the tests, the final crack pattern could not be captured by DIC and can only be inferred from the final photographs (A and C). Before failure, cracks grew from one of the top three head joints and found their way downwards, initially by following the mortar joints, but sooner or later, by cutting the bricks. This is illustrated in Fig. 9 where the progression of the cracks is drawn throughout the test. For many specimens, the cracks could not be reliably detected in the first or the first two steps (i.e. until cycle 60) and hence no crack is shown. Moreover, the detected crack width does not always match the CMOD-controlled value. This is because multiple head joints are cracked simultaneously (see Samples C and D) and together amount to the set opening (defined crack mouth); later, one of the joints progresses while the other unloads. Nonetheless, the progression of the cracks is clearly visible during the final monotonic part of the tests (beyond cycle 90) until failure. These parts evidence how for some specimens (B, C and E), failure occurred progressively, while for specimens A and D, failure was too sudden to be controlled. As seen later in Fig. 10, eventual failure was brittle in all cases.

The sudden failure of specimen D, for example, can also be seen in Fig. 10, where the force-CMOD of the spandrels is shown. Figure 10 also evidences how the strength degradation that occurs during the cyclic steps is due to an accumulation of plastic, irreversible CMOD deformation at the lower force limit value of 2 kN, possibly due to sliding at the crack interfaces. The slope (stiffness) of each cycle is mostly unaffected.



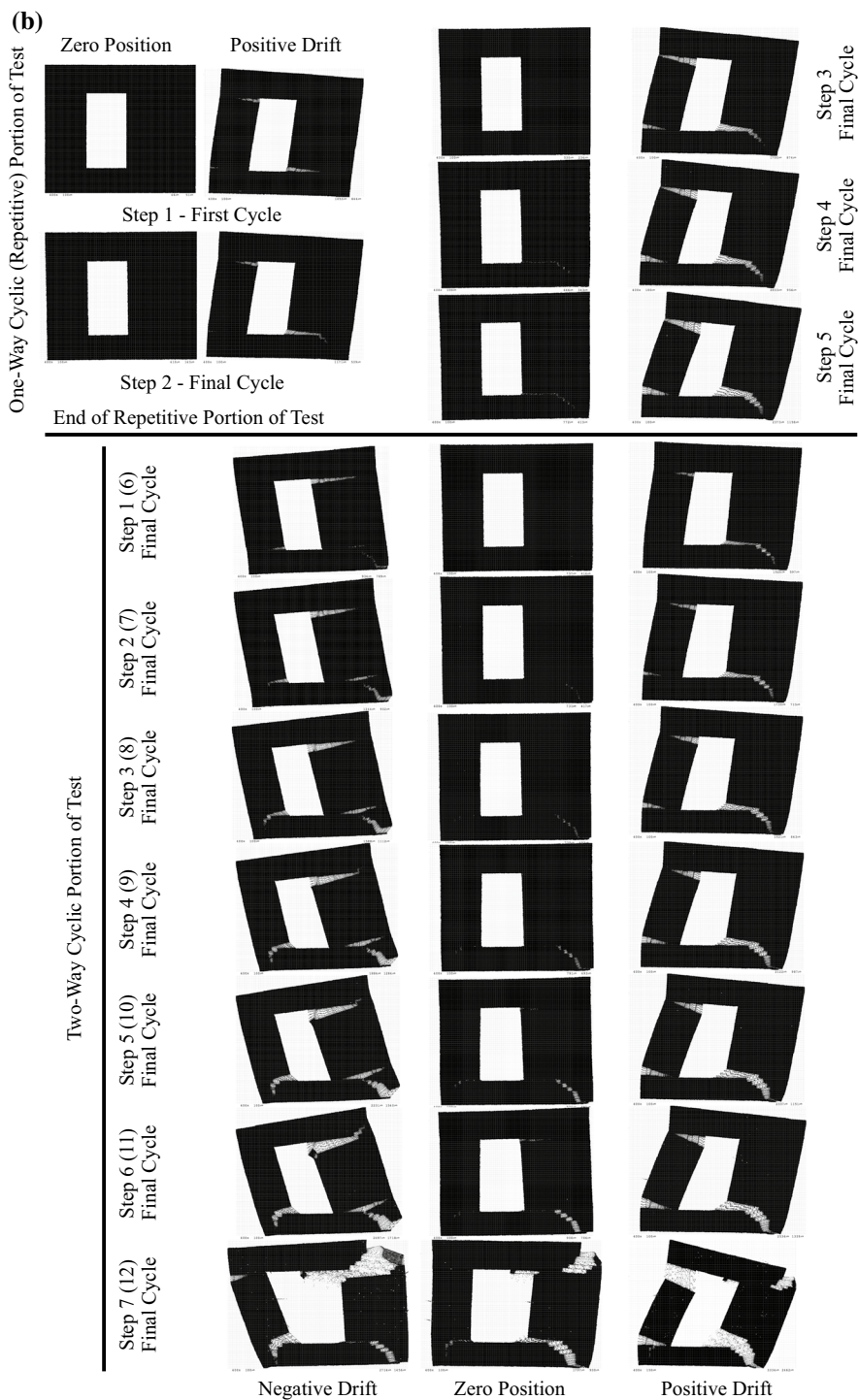
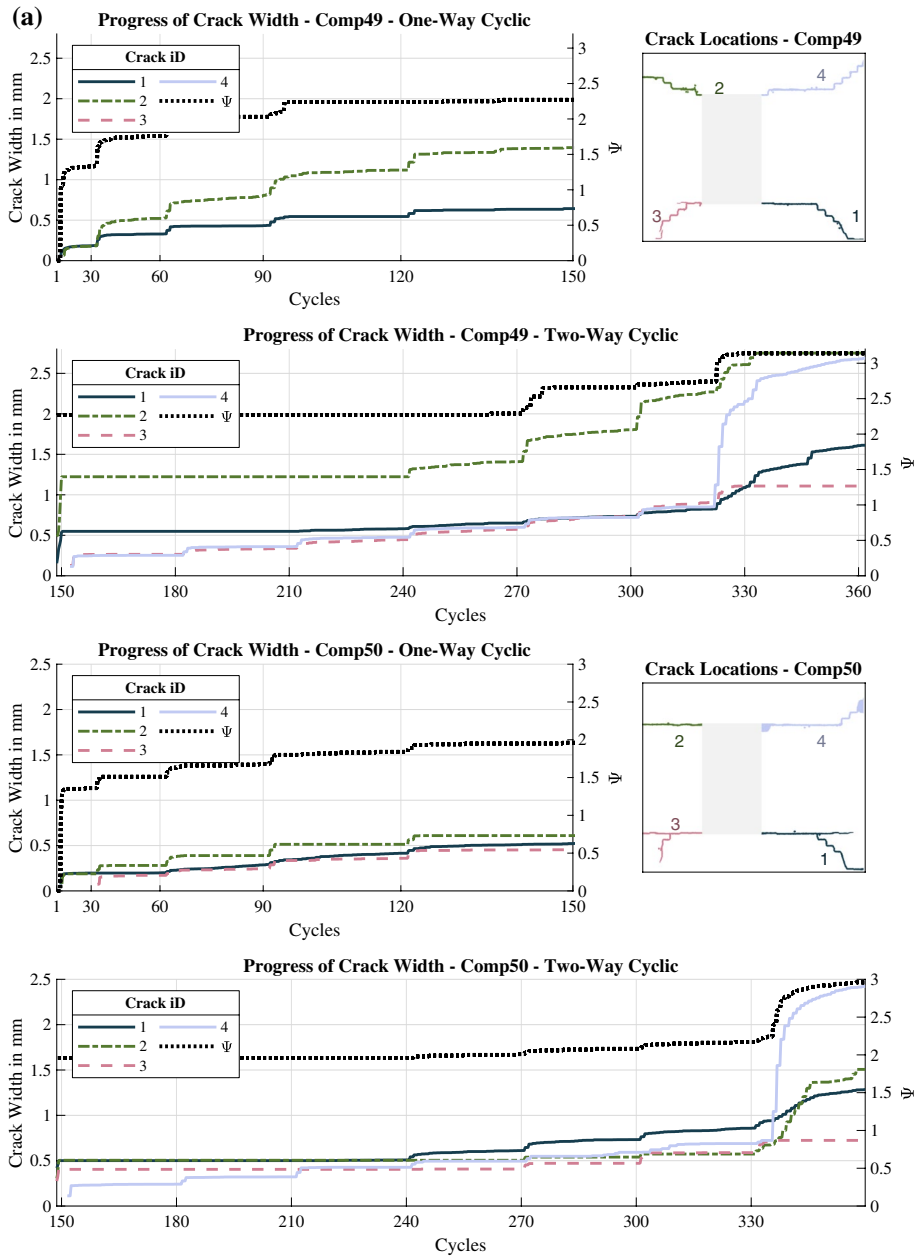


Fig. 6 (continued)



**Fig. 7** **a** Progression of crack width for the full-scale walls. Maximum crack width of each crack for the entire cycle. Note that  $\Psi$  is drawn on the right axis and corresponds to the damage intensity of the entire specimen. Top: Comp49; bottom: Comp50. **b** Progression of crack length for the full-scale walls. Top: Comp49; bottom: Comp50. Note that  $\Psi$  is drawn on the right axis and corresponds to the damage intensity of the entire specimen

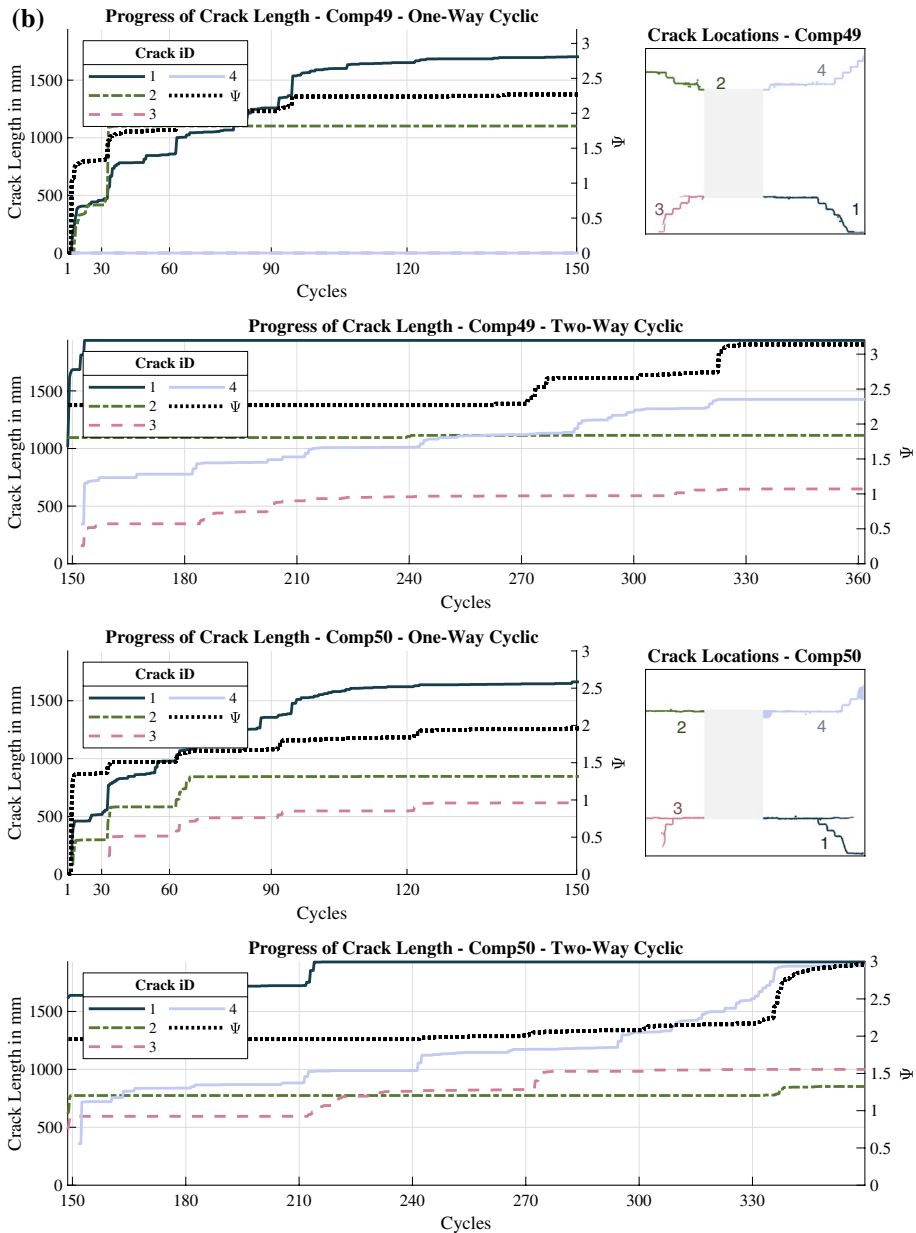
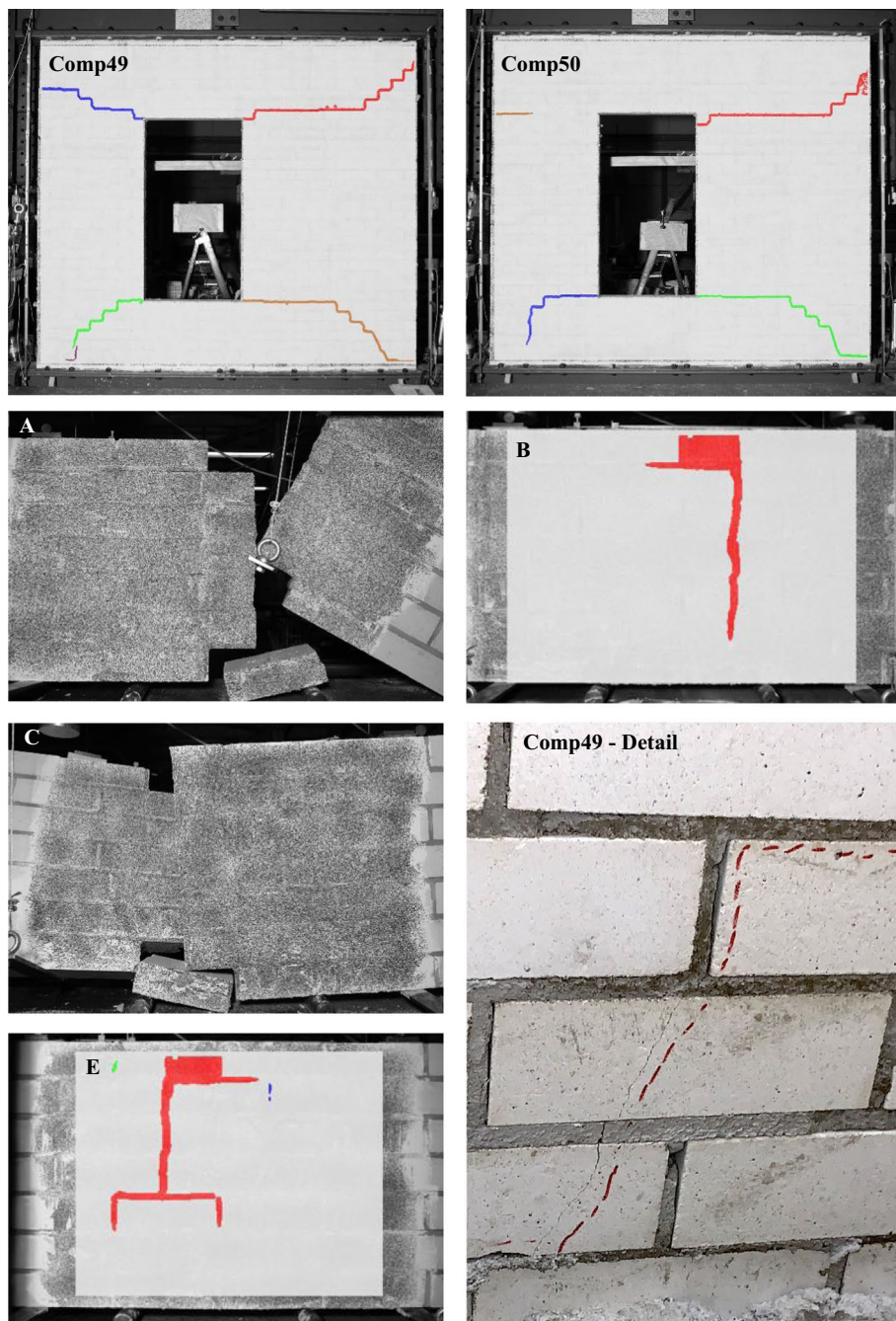


Fig. 7 (continued)

The strength degradation is extremely consistent during the five tests with an average of 15% reduction in capacity at the last, third step. Here, the stabilisation of the degradation effect can also be observed to occur after approximately 30 cycles within the steps, a value that was chosen precisely for this reason. The ultimate capacity of most samples is also consistent, with an average of 32 kN and a standard deviation of





**Fig. 8** Crack patterns showing brittle behaviour of walls top) and four of the five spandrels. Spandrels A and C are shown after failure, while spandrels B and E are overlaid with the detected crack path right before failure. Bottom right: backside of Comp49 showing real crack on the left of dashed highlight

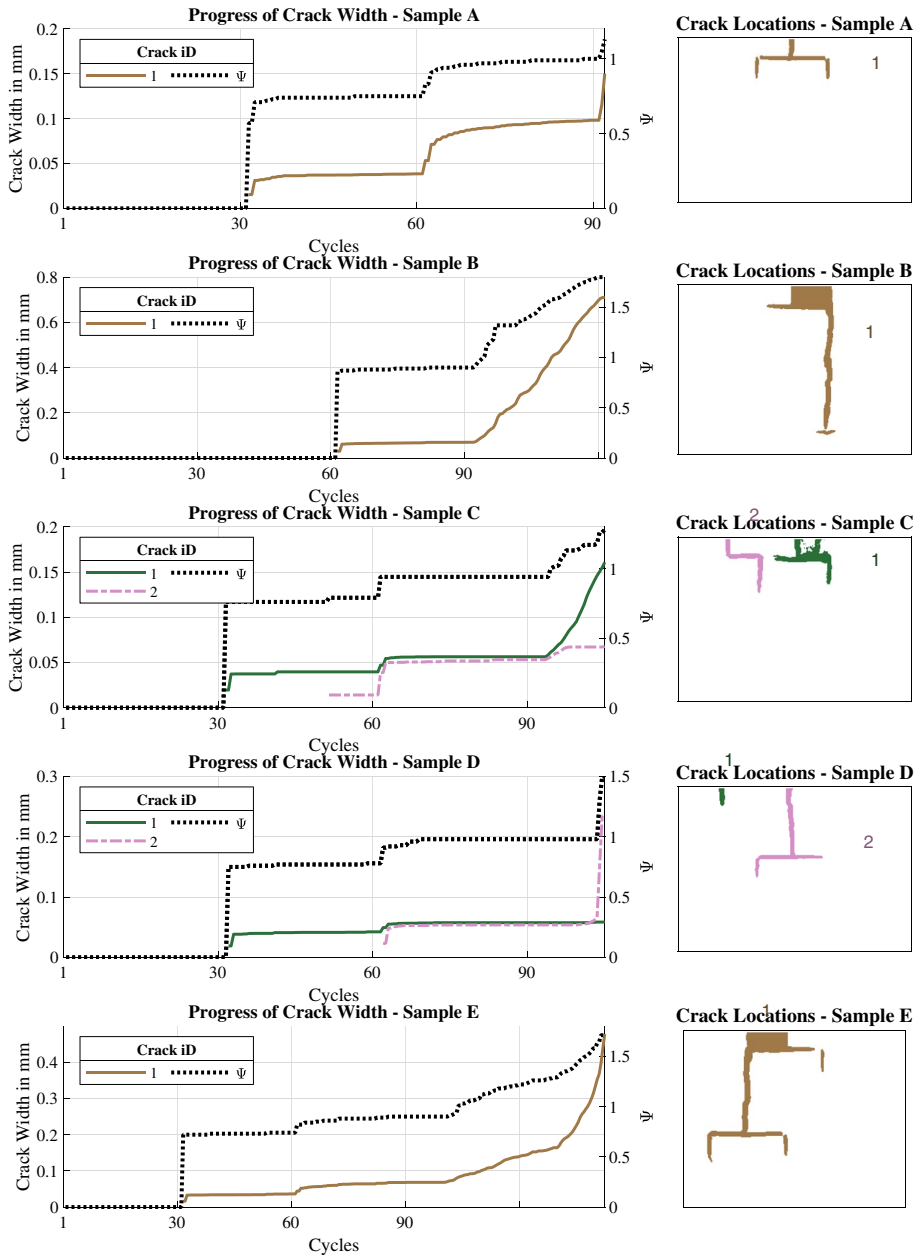


**Fig. 9** Progression of crack width for the spandrel tests during 90 loading cycles and a final monotonic phase

1.9 kN. In spite of the remarkably consistent tests, specimen D showed some dissimilitude: first, the residual plastic deformation was significantly higher than in the other tests; second, the plastic displacement of the first step was negligible, almost zero; and third, the cycles of the last step had a higher strength than the previous cycles



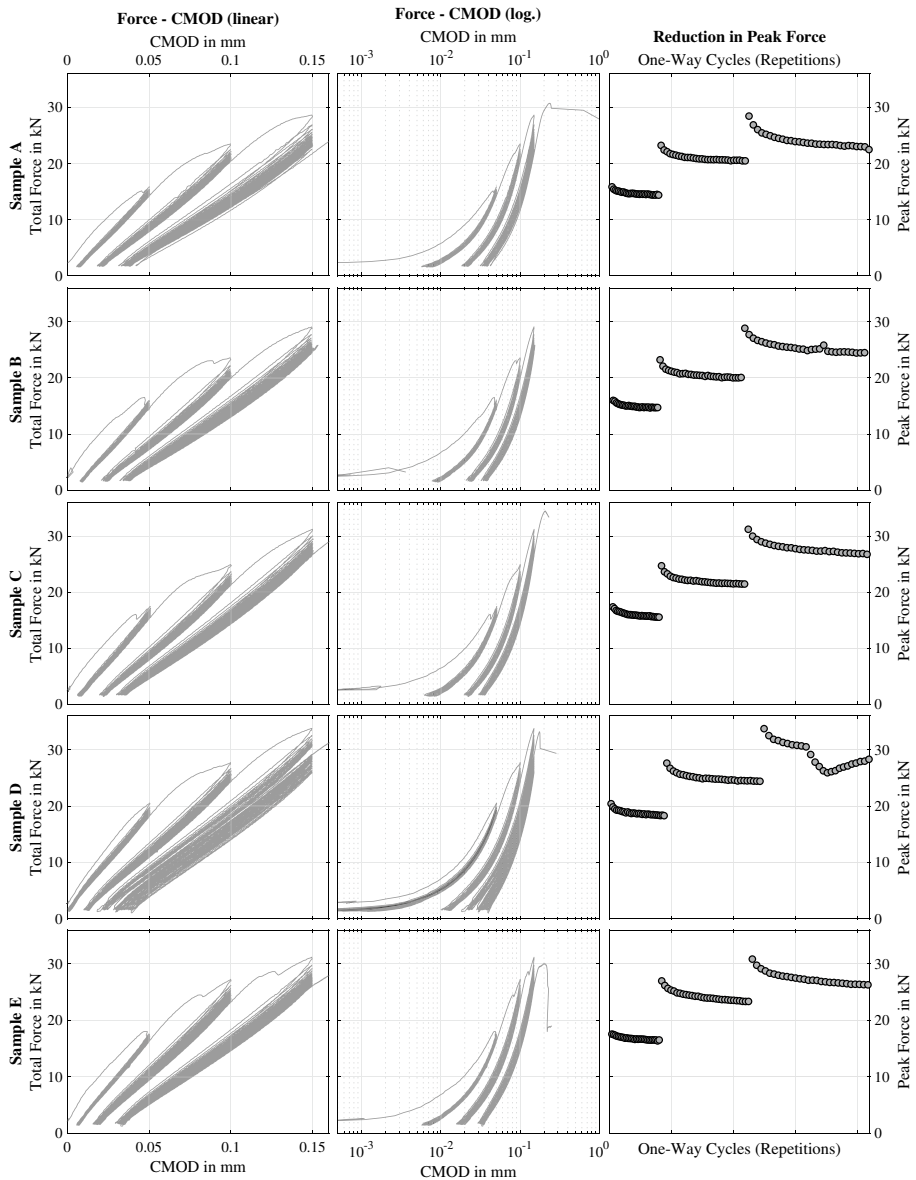


**Fig. 10** Force against CMOD for spandrels tests, plotted linearly showing the cyclic steps (left), and logarithmically showing the entire test (middle). The force reduction identified via the peak of each cycle is also shown (right)

(see erratic behaviour of force peaks, right in Fig. 10). It has not been possible to find a sensible explanation for this behaviour, albeit an out-of-plane influence cannot be neglected in this case.

#### 4 Comparison against clay samples

The two calcium-silicate walls were stiffer and stronger than all of their clay counterparts: This is visible in Fig. 11, where the absolute envelopes (positive and negative loading) of all the cyclic test results for all the tested walls are drawn (though only the area delimited by the CaSi walls is shown shaded for easier identification). The part of the envelope produced by the first step of the calcium-silicate walls is noticeably stiffer than the clay specimens, see peaks of shaded envelope area. Moreover, the calcium walls are stronger in both positive and negative directions. Nonetheless, the calcium-silicate walls experienced more damage at similar drift-values; this is particularly evident by the larger area contoured by the envelopes, indicating a higher hysteresis energy. This is also related to the total cyclic degradation which is higher for the calcium-silicate walls. Yet, the strength degradation during each step, as depicted by the jagged drops in the curves, is comparable for both clay and calcium-silicate specimens.

The increased damage of calcium-silicate walls is also observable in the crack patterns of these specimens when compared to the clay walls. Figure 12 shows five clay walls where cracks are spread into a larger number of individual cracks, and follow predominantly diagonal patterns of off the window corners. Figure 12 displays a cumulative summary of all cracks throughout the entire tests, hence, in contrast, the two calcium-silicate walls display only four cracks which propagate first horizontally from the window corners, then diagonally, and later run vertically through the bricks. The splitting of bricks was something only observed in the calcium-silicate specimens. In fact, spandrel tests, which were to mimic a vertical crack underneath the window bank of the walls, also displayed no brick-splitting in the clay material, but did allow for this brittle failure mechanism in the calcium-silicate specimens. Figure 13 shows that the vertical crack in CaSi spandrel

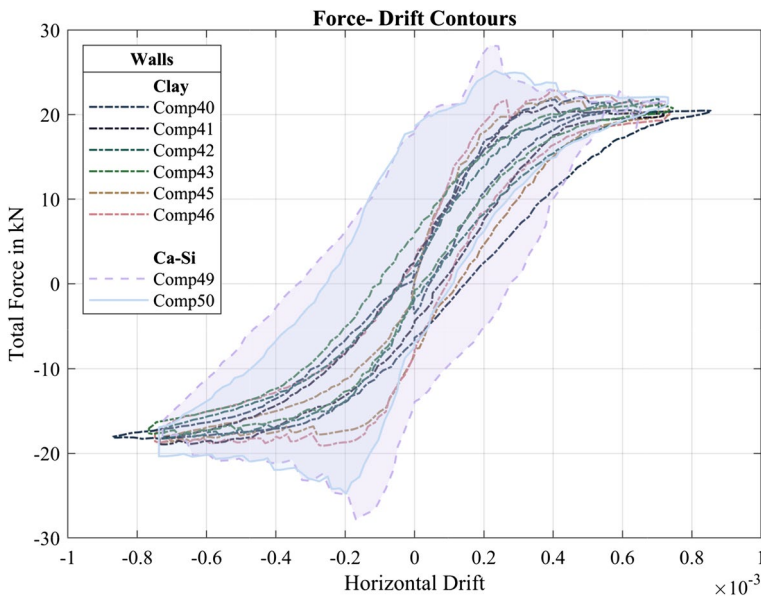


**Fig. 11** Comparison of absolute envelopes (contours) between similar clay walls (dash-dotted) and the two calcium-silicate walls (shaded areas)

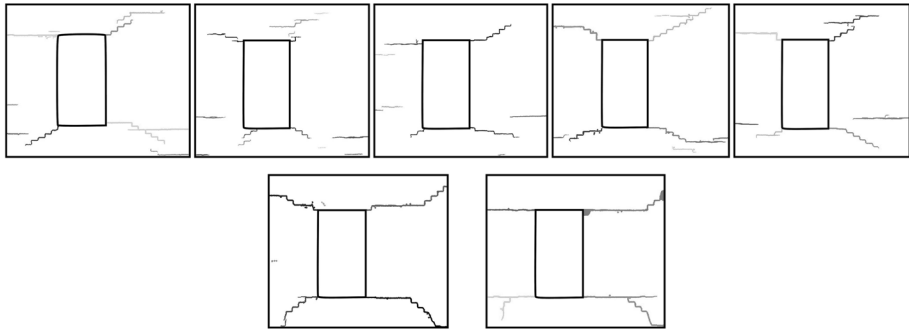


**Fig. 12** Comparison of cumulative crack patterns between 5 clay walls (top) and 2 Ca–Si specimens (bottom). This is a summary of all cracks detected throughout the tests

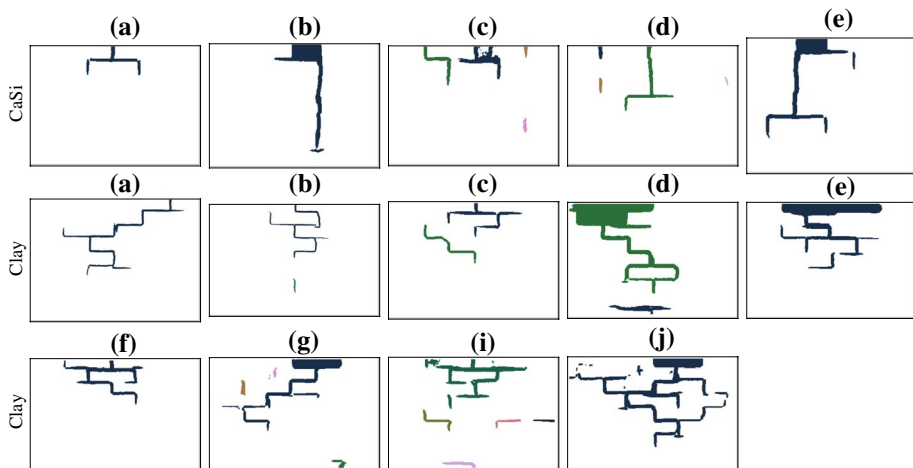


**Fig. 13** Comparison of final crack patterns between calcium-silicate spandrels (top five) and clay specimens (bottom nine)

samples did cut straight down, while the vertical crack of identically-tested clay specimens, zigzagged down forming a toothed crack with complex patterns and bifurcations.

The precise cause for the splitting of bricks in the calcium-silicate specimens while no splitting occurred in clay specimens is not clear; however, a stronger bond between calcium-silicate bricks and its cement mortar, and weaker yet stiffer bricks are forefront hypotheses. In both cases, solid bricks were used. Nonetheless, the consequences of this are clear: calcium-silicate samples experience increased damage with noticeably wider cracks which, moreover, cannot be hidden or easily repaired as they cut bricks, necessitating the replacement of the calcium-silicate unit for a full repair, while for clay, only repointing of the joints is necessary. Note that this is valid for the masonry tested in this study, see Table 2 for a summary of their properties.

The higher sensitivity to damage of this type of calcium-silicate masonry is further expressed in Fig. 14, where the damage values, as computed with the  $\Psi$  parameter, are shown for numerous values of drift. The maximum value of  $\Psi$  is computed for each cycle

**Table 2** Additional properties for calcium-silicate masonry and its components as tested from companion tests and used in this study

Property	Symbol	Mean	Unit	CoV (%)
Compressive strength of mortar	$f_m$	5.68	MPa	9
Flexural strength of mortar	$f_{mt}$	2.32	MPa	13
Normalised compressive strength of Calcium-silicate brick prescribed by producer	$f_b$	11.87	MPa	2
Flexural strength of brick	$f_{bt}$	1.77	MPa	1
Elastic modulus of brick from bending test	$E_b$	3902	MPa	19
Compressive strength of masonry in the direction perpendicular to bed joints	$f'_m$	7.66	MPa	7
Elastic modulus of masonry in the direction perpendicular to bed joints—initial, middle, and end-of-slope	E1	5387	MPa	12
	E2	6995	MPa	12
	E3	4835	MPa	12
Poisson ratio of masonry in the direction perpendicular to bed joints	$\nu$	0.22	—	14
Fracture energy in compression for loading perpendicular to bed joints	$G_{f-c}$	16.25	N/mm	18
Masonry bending strength with the moment vector orthogonal to the plane of the wall	$f_{c,3}$	0.59	MPa	7
Youngs modulus from IP bending	$E_{f,3}$	3705	MPa	13
Flexural bond strength	$f_w$	0.43	MPa	16
Masonry (bed joint) initial shear strength	$f_{c0}$	0.33	MPa	32
Masonry (bed joint) shear friction coefficient	$\mu$	0.64	—	5
Residual masonry (bed joint) initial shear strength	$f_{c0, res}$	0.07	MPa	
Residual masonry (bed joint) shear friction coefficient	$\mu_{per}$	0.59	—	

See also Jafari and Esposito (2019)

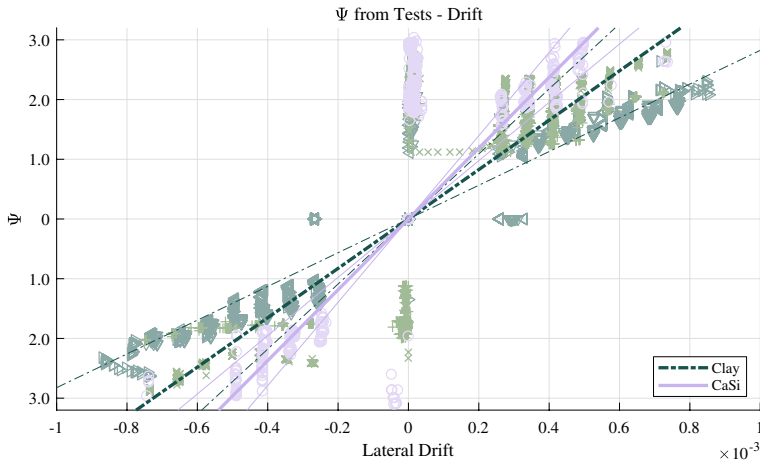


**Fig. 14** Linear regression of the relationship between (non-zero) drift and damage measured in  $\Psi$  for clay and calcium-silicate (CaSi) walls at zero, positive and negative drift values for each cycle. Thinner lines show one standard deviation. Circles show CaSi data while angular shapes show clay data

at the zero position and positive and negative directions (see also Fig. 6). First, in Fig. 14, the values corresponding to calcium-silicate walls reach values higher than any of the clay walls. Moreover, residual damage (at or close to zero drift) also displays a larger value of  $\Psi$ . Furthermore, a linear regression using the Theil–Sen method of slope fitting (Theil 1950) is produced for all the non-zero data. This fit does not consider that walls are progressively damaged during the cyclic steps; yet, it is clear that calcium-silicate walls have a steeper drift-damage relationship. If the range of  $1 < \Psi < 3$  is considered as DS1 (Korswagen et al. 2019), damage starts to be detectable at drift values of 0.25‰ and corresponds to DS1 until 1.1‰ for the clay walls, while, for the calcium-silicate cases, DS1 appeared already at values between 0.15 and 0.65‰. These values consider the one-standard deviation shown.

The flexural strength of the masonry composite material can be computed from the spandrel tests in a way similar to the standard four-point bending test. Here, calcium-silicate samples average a value of 0.6 MPa with a variation of 7%, while their clay counterparts reach 0.5 MPa in average with a variation of 24%. This difference in strength and the fact that calcium-silicate spandrels are also stiffer can be observed in Fig. 15 where the envelopes of the force-CMOD as presented in Fig. 10 are compared to the previously tested clay specimens. Yet, the strongest observation is that calcium-silicate specimens are significantly more brittle than the clay ones. All calcium-silicate specimens reached (sudden) failure at approximately 0.25 mm of crack width, while some clay samples could be tested up to 5 mm of crack width, way beyond DS1 (note that some clay tests were purposely stopped at 0.5 mm). If the vertical crack produced by the spandrel tests belongs to the window bank (ground floor spandrel) of a structure, the calcium-silicate material would be more vulnerable to exceeding DS1. This had also been qualitatively shown in Fig. 13. Furthermore, in Fig. 16, the total force is plotted against the average vertical displacement at the jacks, rather than the CMOD, which allows an estimation of the fracture energy of the tests. Assuming an idealised straight vertical crack with a length of 0.5 m and a thickness of 0.1 m, the energy input by the setup can be interpreted as the mode-I tensile fracture energy ( $G_{\text{II}}$ ) of the composite

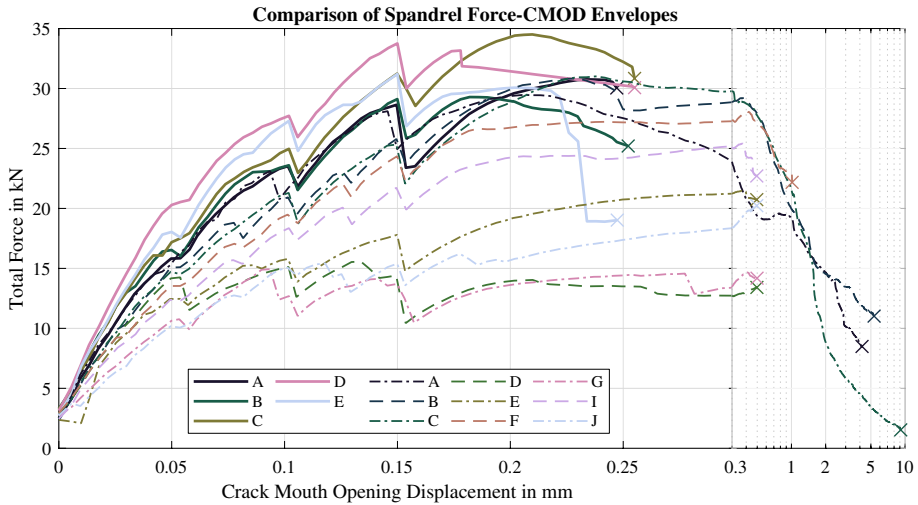


**Fig. 15** Comparison of force–displacement (CMOD) envelopes between spandrel tests of calcium-silicate brick (solid lines) and clay brick (interrupted lines) masonry

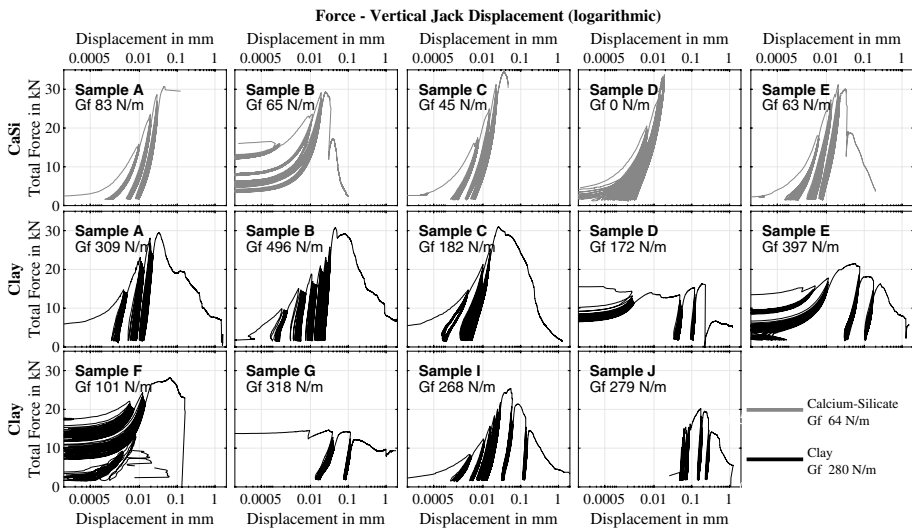


**Fig. 16** Force-displacement (vertical at jacks, not CMOD) for spandrels showing the interpreted tension fracture energy ( $G_f$ )

material. This parameter can serve to further compare the materials. Here, neglecting sample D of the calcium-silicate tests which reached failure early on, the average of the clay spandrels is 4 times higher than the value of  $64 \text{ N m/m}^2$  calculated from the calcium-silicate tests (see Table 3 for a summary). This confirms the more brittle behaviour of this type of calcium-silicate brick masonry in comparison to the replicated clay brick masonry of this study. The larger value for clay is possibly due to the sliding and

**Table 3** Summary of parameters obtained from cyclic spandrel tests for calcium-silicate and clay masonry

Description	Maximum capacity	Flexural strength	Direct tensile strength	Stiffness	Mode-I Composite fracture energy
Symbol	$F_{\max}$	$f_{x3}$	$f_t$	E	$G_{fl}$
Material	kN	MPa	MPa	MPa	Nm/m <sup>2</sup>
Calcium-silicate	31.9 (6%)	0.59 (7%)	0.27 (15%)	3705 (13%)	64 (24%)
Clay	24.2 (24%)	0.52 (24%)	0.24 (12%)	3199 (25%)	280 (43%)

Average and percentual deviation (coefficient of variation) shown

interlocking occurring between bricks, where the CaSi tests reveal mode-I crack through bricks and joints.

Moreover, the high values in comparison to literature (35 N/m from NEN 2018, for clay and 15 N/m for calcium-silicate) are likely because of the cyclic nature of the tests which allow a larger amount of energy to be released through hysteresis, the interlocking occurring in this type of clay masonry, and the back-and-forth sliding of the bed joints in the cyclic test. The monotonic clay window bank tests (not included in this study but part of previous investigations) averaged 80 N/m, indicating that about 70% of the measured energy corresponds to the cyclic nature of the test. Still, this value remains high when compared to literature and this is to be attributed to the sliding (instead of splitting) of clay bricks, suggesting dependence between the failure mechanism and the property of fracture energy. In this sense, the fracture energy obtained from the cyclic tests is not a real material parameter since it not only includes the generation of the fracture surface but also the intermediate energy accumulated during the sliding; consequently, it should only be used as a comparison, in this case, between clay and calcium-silicate masonry. Nevertheless, the dependence of the fracture energy property and the failure type of the material remains as an important observation; additional investigations should be performed to determine what combinations of mortar and brick properties and geometries, and the bond between them, lead to the brittle or the more robust failure mechanism.

## 5 Conclusions

This study has looked into the experimental results of two full-scale masonry walls and five spandrels built of calcium-silicate brick and compared these to similar specimens of baked-clay brick, both materials representative of unreinforced masonry structures in the Netherlands. The loading protocols employed were designed to assess the influence or repeated, light earthquakes. In contrast to the type of clay masonry selected, calcium-silicate samples were stiffer and slightly stronger. Yet, at similar values of in-plane, lateral drift, they exhibited more light damage, measured by the width of the cracks. Since the material is stiffer, the increased damage was not unexpected, but, the samples also displayed a more brittle behaviour, with bending and splitting cracks running through the bricks, something not seen in any of the clay experiments where cracks follow the mortar joints. This seems to indicate that walls built of calcium-silicate brick are more vulnerable to light damage especially since these splitting cracks are more difficult to hide or repair, necessitating the replacement of the brick units. Similar walls of the clay material employed in this study



where not as vulnerable. According to the present tests with only one geometry of walls and limited to the selected masonry materials, light damage for calcium-silicate walls acting mainly in flexure is thus expected between drift values of 0.15 and 0.65%.

**Acknowledgements** This research was funded by Nederlandse Aardolie Maatschappij (NAM) under Contract No. UI67339 ‘Damage sensitivity of Groningen masonry building structures—Experimental and computational studies’, contract holders: Jan van Elk and Jeroen Uilenreef. This cooperation is gratefully acknowledged. The authors also express their gratitude to Edwin Meulman for his extensive support in designing, conducting and interpreting the laboratory experiments.

**Open Access** This article is licensed under a Creative Commons Attribution 4.0 International License, which permits use, sharing, adaptation, distribution and reproduction in any medium or format, as long as you give appropriate credit to the original author(s) and the source, provide a link to the Creative Commons licence, and indicate if changes were made. The images or other third party material in this article are included in the article’s Creative Commons licence, unless indicated otherwise in a credit line to the material. If material is not included in the article’s Creative Commons licence and your intended use is not permitted by statutory regulation or exceeds the permitted use, you will need to obtain permission directly from the copyright holder. To view a copy of this licence, visit <http://creativecommons.org/licenses/by/4.0/>.

## References

- Crowley H, Pinho R, Van Elk J, Uilenreef J (2018) Probabilistic damage assessment of buildings due to induced seismicity. *Bull Earthq Eng*. <https://doi.org/10.1007/s10518-018-0462-1>
- de Vent I, Rots JG, van Hees RPJ (2011) Structural damage in masonry—developing diagnostic decision support. TU Delft, Delft
- den Bezemer T, van Elk J (2018) Special report on the Zeerijp Earthquake—8th January 2018. NAM
- Esposito R, Messali F, Ravenshorst GJP, Schipper HR, Rots JG (2018) Seismic assessment of a two-storey unreinforced masonry Dutch terraced house. *Bull Earthq Eng* 17:4601–4623
- Graziotti F, Rossi A, Mandirola M, Penna A, Magenes G (2016) Experimental characterisation of calcium-silicate brick masonry for seismic assessment. In: 16th international brick and block masonry conference. ISBN 978-1-138-02999-6
- Graziotti F, Tomassetti U, Kallioras S, Penna A, Magenes G (2017) Shaking table test on a full scale URM cavity wall building. *Bull Earthq Eng* 15(12):5329–5364
- Grünthal G, Musson RMW, Schwarz J, Stucchi M (1998) European Macroseismic Scale 1998 (EMS-98). European seismological commission, sub commission on engineering seismology, working group macroseismic scales. Conseil de l’Europe, Cahiers du Centre Européen de Géodynamique et de Séismologie, vol 15, Luxembourg
- Hendry EAW (2001) Masonry walls: materials and construction. *Constr Build Mater* 15(2001):323–330
- Jafari S, Esposito R (2019) Summary of material properties of existing Dutch masonry—updated URM abacus (version 2). Delft University of Technology. Report no. C31B67WP1-16, version 02
- Jafari S, Esposito R, Rots JG, Messali F (2017) Characterizing the material properties of Dutch unreinforced masonry. *Proc Eng* 193:250–257
- Jonaitis B, Marciukaitis G, Valivonis J (2009) Analysis of the shear and flexural behaviour of masonry with hollow calcium silicate blocks. *Eng Struct* 31:827–833
- Korswagen PA, Meulman E, Longo M, Rots JG (2018) Crack initiation and propagation in unreinforced masonry structures subjected to repeated load and earthquake vibrations. In: 10th international masonry conference, Milan
- Korswagen PA, Longo M, Meulman E, Rots JG (2019) Crack initiation and propagation in unreinforced masonry specimens subjected to repeated in-plane loading during light damage. *Bull Earthq Eng*. <https://doi.org/10.1007/s10518-018-00553-5>
- Magenes G, Morandi P, Penna A (2012) In-plane cyclic tests of calcium silicate masonry walls. In: 14th international brick and block masonry conference, Sydney
- Messali F, Esposito R, Jafari S, Ravenshorst G, Korswagen PA, Rots JG (2018) A multiscale experimental characterization of Dutch unreinforced masonry buildings. In: 16th European conference on earthquake engineering, Thessaloniki

- Messali F, Rots JG (2018) In-plane drift capacity at near collapse of rocking unreinforced calcium silicate and clay masonry piers. *Eng Struct* 164(2018):183–194
- Mojilović N, Salmanpour AH (2016) Masonry walls subjected to in-plane cyclic loading: application of digital image correlation for deformation field measurement. *Int J Masonry Res Innov* 1(2):165
- NAM (2016) Production, subsidence, induced earthquakes and seismic hazard and risk assessment in the groningen field. NAM, Technical Addendum to the Winningsplan Groningen. [www.NAM.nl](http://www.NAM.nl)
- NEN (2018) Nederlandse Praktijkrichtlijn (NPR) 9998—Dutch guideline of practice. NEN
- Petry S, Beyer K (2015) Limit states of modern unreinforced clay brick masonry walls subjected to in-plane loading. *Bull Earthq Eng* 2015(13):1073–1095. <https://doi.org/10.1007/s10518-014-9695-9>
- Sarhosis V, Dais D, Smyrou E, Bal IE (2019) Evaluation of modelling strategies for estimating cumulative damage on Groningen masonry buildings due to recursive induced earthquakes. *Bull Earthq Eng*. <https://doi.org/10.1007/s10518-018-00549-1>
- Theil H (1950) A rank-invariant method of linear and polynomial regression analysis. I, II, III. *Nederl Akad Wetensch Proc* 53:386–392, 521–525, 1397–1412
- Thijssen CCF (1999) *Bouwconstructieve Analyse Van Naoor-Logse Eengezinsbui-Zen in De Non-profit Huursector 1946–1980*. Delft University of Technology Press
- Van Staalduinen PC, Terwel K, Rots JG (2018) *Onderzoek naar de oorzaken van bouwkundige schade in Groningen Methodologie en case studies ter duiding van de oorzaken*. Delft University of Technology. Report number CM-2018-01, 11 July 2018. [www.NationaalCoördinatorGroningen.nl](http://www.NationaalCoördinatorGroningen.nl)

**Publisher's Note** Springer Nature remains neutral with regard to jurisdictional claims in published maps and institutional affiliations.